bioRxiv preprint doi: https://doi.org/10.1101/2022.04.19.488747; this version posted April 19, 2022. The copyright holder for this preprint (which was not certified by peer review) is the author/funder, who has granted bioRxiv a license to display the preprint in perpetuity. It is made available under aCC-BY-NC-ND 4.0 International license.

ISM-FLUX: single-step MINFLUX with an array detector*

Eli Slenders and Giuseppe Vicidomini†
Istituto Italiano di Tecnologia, Genova, Italy

(Dated: April 19, 2022)

Single-molecule localization based on the concept of MINFLUX allows for molecular resolution imaging and tracking. However, MINFLUX has a limited field-of-view and therefore requires a precise and photon-costly pre-localization step. We propose ISM-FLUX, a localization technique that combines structured illumination with structured detection. We show through simulations that replacing the point-detector with a small (e.g. 5×5 pixels) single-photon camera and sequentially exciting the sample with four spatially separated doughnut-shaped beams, a localization precision between 1 and 15 nm can be obtained over a field-of-view (FOV) of more than 800 nm with 100 photons. The large FOV, induced by the camera, makes the pre-localization step obsolete. We calculate the effect of different parameters, such as the position of the doughnut beams and the number of pixels, on the localization precision. We predict that the combination of a good localization precision and the experimental simplicity of ISM-FLUX will help the wide adoption of MINFLUX based microscopy.

Localizing single fluorescent molecules with nanometer precision is key for both single particle tracking and imaging beyond the diffraction limit. Nowadays, most techniques fall in either of two categories: structured detection (SD) or structured illumination (SI) based localization. The former category includes all techniques in which a sparse subset of the fluorescent molecules is active, illuminated with wide-field illumination, and imaged with a large camera. After analysing the emission patterns to find the fluorophore coordinates, the process is repeated with a different subset until a sufficient number of fluorophores has been localized. Most implementations of conventional single molecule localization microscopy (SMLM), such as direct stochastic optical reconstruction microscopy (dSTORM) [1, 2], photoactivated localization microscopy (PALM) [3, 4], and points accumulation for imaging in nanoscale topography (PAINT) [5] are examples of SD localization. These techniques can be implemented on conventional low-cost wide-field camera-based setups and can be used for large field-of-view (FOV) imaging of live samples while, at the same time, giving quantitative information on the cellular organization and functioning at the molecular level [6, 7]. However, the localization precision scales with $\sqrt{N}$, with N the number of fluorescence photons. As a result, long acquisition times may be required for a good localization, making these techniques prone to photobleaching and sample drift. In addition, the fluorescence pattern, and hence the calculated fluorophore position, is affected by the orientation of the emission dipole [8]. While SD localization can reach unlimited resolution in theory, these factors typically limit the localization precision to about 20-50 nm in practice [9], although precisions below 5 nm have been reported [10, 11]. Furthermore, emCCD or sCMOS cameras used in SMLM suffer from read-out, thermal, and electronic noise and usually have a maximum frame rate in the kHz range, making this detection method incompatible with time-domain lifetime imaging, although this limitation could be solved with other camera types [12, 13].

In SI localization, on the other hand, the information on the fluorophore's position is entirely encoded in the excitation pattern. These techniques require a set of illumination patterns, typically doughnut shaped beams focused at different positions around a single active fluorophore, following a pre-defined pattern, called the targeted coordinate pattern (TCP). For each position in the TCP, the fluorescence intensity is recorded with a single point-detector and analyzed to find the fluorophore's position. Localization techniques based on SI, such as MINFLUX [14], MINSTED [15], pMINFLUX [16], and two-photon MINFLUX [17] can reach precisions of a couple of nanometers with a much smaller emission photon budget in comparison to SD techniques and the precision does not depend on the emission wavelength or the molecular orientation. In addition, single point-detectors, such as avalanche photodiodes (APD), provide shot–noise limited detection and allow combining localization microscopy with time-correlated single-photon counting (TC-SPC), for example for measuring the lifetime [18] or for quantum microscopy. However, by spatially integrating all photons with a single-point detector, some information on the molecule's position gets lost. This is particularly problematic when the molecule is outside the region spanned by the TCP [19], as the likelihood function may show multiple local maxima far away from the actual fluorophore position. In typical SI implementations, this lack of robustness demands a precise and photon costly pre-localization procedure to make sure that the active fluorophore is inside the TCP [20].

Here, we propose a molecule localization technique that takes inspiration from MINFLUX and image scanning microscopy (ISM) [21, 22]. Our technique, called ISM-FLUX, combines structured illumination – by

* Preprint
† giuseppe.vicidomini@iit.it

bioRxiv preprint doi: https://doi.org/10.1101/2022.04.19.488747; this version posted April 19, 2022. The copyright holder for this preprint (which was not certified by peer review) is the author/funder, who has granted bioRxiv a license to display the preprint in perpetuity. It is made available under aCC-BY-NC-ND 4.0 International license.

means of spatially displaced doughnut shaped beams that sequentially excite the sample – with structured detection – by using a fast camera. We calculate the Cramér-Rao bound for different experimental parameters, such as the diameter of the targeted coordinate pattern, the signal-to-background ratio (SBR), the magnification, and the number of pixels to show the effect on the theoretical localization precision that can be expected in each case and to find the optimal experimental settings. We pay particular attention to the case of localizing fluorophores outside of the TCP, since this is the main bottleneck of conventional MINFLUX based techniques and could be overcome by using a camera. Note that the combination of SI and SD for localizing molecules has been demonstrated before [23, 24] but in these techniques the three standing wave illumination patterns (for each orientation) are laterally shifted with respect to each other by one third of the pattern pitch, limiting the resolution improvement to about a factor of two with respect to conventional SMLM.

In the proposed experimental setup, Fig. 1, an activation laser turns on a single fluorophore, which is then excited with a series of four laterally displaced doughnut beams, where the displacements are in the order of 12 to 250 nm. The activation step can be skipped for imaging methodologies that do not require photo-activation, such as PAINT, or can be replaced with an off-switching procedure, *e.g.* for dSTORM. The position of each doughnut beam is predefined, *i.e.*, it does not have to be updated during the experiment in a feedback loop, hence the description "single-step MINFLUX". The beams can be focused at different positions by splitting the excitation beam into four beams and aligning each beam with a different set of mirrors or by means of a spatial light modulator. Here, we assume a TCP consisting of three equidistant positions on a circle and a fourth position in the center of this circle. Each beam can be sequentially turned on, for example with a set of acousto-optic modulators or by using pulsed interleaved excitation (PIE). The resulting fluorescence is collected and focused onto a small single-photon camera, *e.g.* a single-photon avalanche diode (SPAD) array detector consisting of a matrix of 5×5 or 7×7 pixels. The detector is connected to a data acquisition system with a high enough temporal resolution to link each photon to one of the excitation patterns, *e.g.*, with a TC-SPC module in the case of PIE. The four doughnut beams continuously excite the sample until enough photons have been collected for an accurate localization or until the fluorophore has turned to an off–state. A scanning system with two galvanometric scanners or a scanning stage can be installed to increase the FOV. In the former case, the array detector must be installed in a de-scanned configuration.

A conventional MINFLUX experiment yields four values, corresponding to the emission photon counts for each of the four positions in the TCP. The fluorophore can be localized with a maximum likelihood estimator (MLE), taking into account the combination of the shape and position of the excitation beams with the four photon counts. An ISM-FLUX measurement, on the other hand, does not only provide the number of counts for each position in the TCP but also tells us where in the image plane those photons were detected. ISM-FLUX thus combines the ideas of MINFLUX and conventional single-molecule localization microscopy. Similar to ISM, the detection point-spread-function (PSF) for each pixel of the detector array is laterally shifted with respect to the PSF of the central element. Since the overall molecule detection function (MDF) is the product of the excitation intensity (assuming linearity between the laser intensity and the emitted photon count rate) and the detection PSF, a total of 100 MDFs can be defined for a combination of four doughnut positions and a 5×5 detector array. Note that these 100 MDFs are constant over the experiment and can thus be measured in a reference experiment. Applying the same maximum likelihood procedure as in MINFLUX, but with 100 MDFs instead of 4, yields the fluorophore's coordinates. In particular, the likelihood function $\mathcal{L}(\mathbf{r}_E|\mathbf{n})$ for the fluorophore at position $\mathbf{r}_E$ given $\mathbf{n} = (n_1, n_2, n_3, ..., n_{100})$ photon counts for the $K = 100$ different MDFs can be expressed as

$$\mathcal{L}(\mathbf{r}_E|\mathbf{n}) = \frac{N!}{\prod_{i=1}^{K} n_i!} \prod_{i=1}^{K} p_i(\mathbf{r}_E)^{n_i}, \tag{1}$$

with $N = \sum_{i=1}^{K} n_i$ the total number of detected photons and $p_i(\mathbf{r}_E)$ the probability that a photon is detected by MDF_i, *i.e.*, by one of the 100 combinations of excitation pattern and detector pixel. We assume that both the signal and all background contributions (*e.g.*, out-of-focus signal or dark counts) are Poisson distributed and that the background is equal for all pixels and all excitation patterns. Then,

$$p_i(\mathbf{r}_E) = \frac{\mathrm{SBR}(\mathbf{r}_E)}{\mathrm{SBR}(\mathbf{r}_E+1)} \frac{\mathrm{MDF}_i(\mathbf{r}_E)}{\sum_{j=1}^{K} \mathrm{MDF}_i(\mathbf{r}_E)} + \frac{1}{\mathrm{SBR}(\mathbf{r}_E)+1} \frac{1}{K}. \tag{2}$$

The fluorophore's position can be estimated as $\arg\max \mathcal{L}(\mathbf{r}_E|\mathbf{n})$ or, equivalently, $\arg\max \ell(\mathbf{r}_E|\mathbf{n})$, with $\ell = \ln(\mathcal{L})$ the so-called log–likelihood function.

To obtain an estimate of the precision that can be obtained with this approach, we calculate the Fisher information matrix:

$$F = N \sum_{i=1}^{K} \frac{1}{p_i} \begin{pmatrix} \left(\frac{\partial p_i}{\partial x}\right)^2 & \frac{\partial p_i}{\partial x}\frac{\partial p_i}{\partial y} \\ \frac{\partial p_i}{\partial y}\frac{\partial p_i}{\partial x} & \left(\frac{\partial p_i}{\partial y}\right)^2 \end{pmatrix}. \tag{3}$$

The best obtainable localization precision is given by the Cramér-Rao bound (CRB) and can be obtained from the inverse of the Fisher matrix, which gives a lower

bioRxiv preprint doi: https://doi.org/10.1101/2022.04.19.488747; this version posted April 19, 2022. The copyright holder for this preprint (which was not certified by peer review) is the author/funder, who has granted bioRxiv a license to display the preprint in perpetuity. It is made available under aCC-BY-NC-ND 4.0 International license.

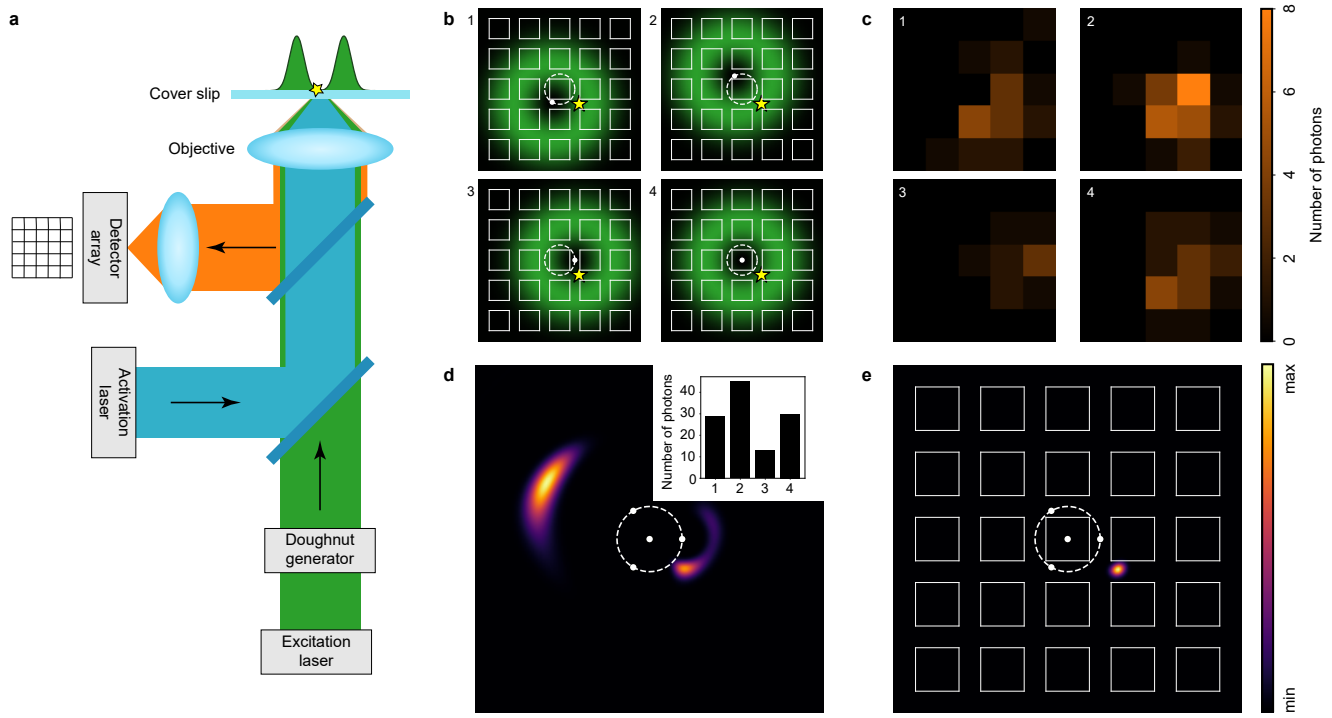

FIG. 1. (a) Concept of ISM-FLUX. An activation laser beam activates a single fluorophore in the sample (yellow star) which is sequentially excited (b) by a series of spatially displaced doughnut beams. (c) The fluorescence for each pattern is imaged with a single-photon array detector. (d-e) Corresponding likelihood functions for the localisation of the fluorophore taking into account (d) only the fluorescence counts for the different patterns (histogram shown in the inset), *i.e.*, conventional MINFLUX, and (e) exploiting the spatial information of the array detector, *i.e.*, ISM-FLUX. Simulation settings: 117 emission photons, pixel size and pixel pitch projected in the sample space 100 nm and 150 nm, respectively, L = 150 nm, 5×5 element detector array. More details in Supplementary Note 2.

bound for the covariance matrix of the localization precision. Here, we take the arithmetic mean of the eigenvalues of the inverse of the Fisher matrix as a performance metric:

$$\sigma_{\mathrm{CRB}}(\mathbf{r}_E) = \sqrt{\frac{1}{2} tr(F^{-1})}. \tag{4}$$

The experimental parameters that the user can control in ISM-FLUX are the diameter of the TCP (L), the optical magnification of the setup (M), the SBR via the excitation power, the number of counts via the combination of pixel dwell time and excitation power, and the number of pixels of the detector. We calculate $\sigma_{\mathrm{CRB}}(\mathbf{r}_E)$ numerically for different values of these parameters and compare the results with conventional "single iteration" MINFLUX, *i.e.*, MINFLUX with a TCP that is not iteratively updated.

The extra spatial information in ISM-FLUX has a significant effect on the likelihood function and, consequently, on the CRB, especially when the fluorophore is outside of the TCP circle, Fig. 1 (b-e). In this example, the likelihood function for ISM-FLUX has a single local maximum close to the actual position of the fluorophore. Instead, for MINFLUX, the likelihood function not only has a peak close to the true position, but there is also a large region about 300 nm away from the fluorophore which, in this case, also contains the global maximum. We found similar results for other fluorophore positions outside of the TCP circle, Fig. S1.

The difference in the likelihood functions is also reflected in the CRB, Fig. 2. *E.g.* for L = 150 nm (*i.e.*, the same TCP diameter as in Fig. 1), both techniques yield very similar and small CRB values for molecules located close to the TCP center: a precision of about 5 nm can be obtained with 100 photons. In fact, one can show (Supplementary Note 1) that under certain conditions the CRB of ISM-FLUX and the CRB of MINFLUX are identical for a molecule on the optical axis. For molecules located farther from the center, the CRB increases. In the case of MINFLUX, the increase happens drastically; the average CRB within a field-of-view (FOV) of 300 nm is more than 40 nm, Fig. 2 (b), compared to about 10 nm for ISM-FLUX. The difference increases significantly with increasing FOV, with ISM-FLUX still having a precision below 15 nm for a FOV of 1 µm, while MINFLUX is ineffective for large FOV's due to regions where the CRB is diverging, Fig. 2 (a). If we consider a more realistic scenario in which the SBR is a function of the fluorophore position, *i.e.*, the closer the molecule is to

bioRxiv preprint doi: https://doi.org/10.1101/2022.04.19.488747; this version posted April 19, 2022. The copyright holder for this preprint (which was not certified by peer review) is the author/funder, who has granted bioRxiv a license to display the preprint in perpetuity. It is made available under aCC-BY-NC-ND 4.0 International license.

the maximum intensity of the doughnut, the more the molecule will be excited and the more emission photons will be detected, ISM-FLUX has a very constant CRB up to a FOV of about 600 nm, Fig. 2 (a, last column) and (c). Within this area, the typical decrease in localization precision for molecules farther away from the TCP is entirely compensated by a simultaneous increase in the SBR, Fig. S2. Outside of this area, the SBR drops and the CRB increases quickly.

Clearly, the main advantage of ISM-FLUX is its localization performance for molecules outside of the TCP circle. As a result, ISM-FLUX, unlike MINFLUX, does not require an accurate pre-localization of the fluorophore. In fact, the only requirement is that the fluorophore is within the camera FOV and excited strongly enough to produce a enough fluorescence photons. For a smart choice of the experimental parameters, these requirements are easily fulfilled and the pre-localization step can be completely skipped. For example, when the camera is large with respect to L, the doughnut size, and the emission PSF, any molecule that is excited is also detected by the camera. And given the homogeneity of the CRB over the FOV, no iterative re-centering procedure is needed. The fact that both the pre-localization step and the iterative process can be skipped saves time and makes ISM-FLUX more economical on the photon budget and easier to implement. To find the optimal experimental conditions, we simulated the effect of several parameters on the CRB.

For small L values and for molecules located close to the optical axis, the MINFLUX CRB and the ISM-FLUX CRB are very similar and small, Fig. 2 (a). For L = 12 nm, the simulations show a precision of about 0.48 nm with 100 photons for a molecule on the optical axis, in good agreement with the analytically calculated value of $L/(2\sqrt{2N}) = 0.43$ nm, Supplementary Note 1. The average CRB within the circle of the TCP is less than 3 nm, both for MINFLUX and ISM-FLUX. However, as L becomes larger, the homogeneity of the MINFLUX CRB worsens dramatically while the ISM-FLUX CRB is much less affected and is still below 15 nm (within the TCP circle) for L = 400 nm. Small L values are thus preferable for both techniques but ISM-FLUX is less prone to the adverse effects appearing at larger L values.

SMLM, single-iteration MINFLUX and ISM-FLUX all have a localization precision that scales with $1/\sqrt{N}$, Fig. S3. However, the absolute values are different for each technique. The precision in SMLM is given by $\sigma_{em}/\sqrt{N}$, with σ_{em} the standard deviation of the emission PSF, assumed to be Gaussian. The user has little control over the precision, other than choosing bright fluorophores and sensitive detectors to maximize N. In comparison, in SI techniques, also the TCP can be user-defined. Hence, comparing the mean CRB within the TCP circle, ISM-FLUX performs more than two times better than SMLM, and about 20% better than MINFLUX. In addition, unlike MINFLUX, ISM-FLUX can also localize molecules with good precision outside of this area, which is a pivotal advantage of ISM-FLUX.

In ISM-FLUX, the fluorescence is detected in descanned mode. Similarly to ISM, the array detector size influences the image or localization performance of the system. The detector size is typically not a tunable parameter but the magnification with which the emission signal is focused onto the array detector can be adjusted. Within the TCP circle, the magnification has almost no effect on the CRB, Fig. S4 (a-b). A high magnification leads to a homogeneous and good localization precision over the whole detector FOV but at the cost of a smaller FOV. The CRB is much more heterogeneous for a low magnification, with values ranging from 4 nm close to the optical axis to more than 100 nm near the detector edges. In addition, with a low magnification, the confocal property to block fluorescence from out-of-focus planes will be lost, which will lead to an increased background signal. A good trade-off is M = 500× (which *e.g.* can be achieved with a 100× objective-tube lens system, followed by an additional 5× magnification), Fig. S4 (c). This configuration, which is similar to a conventional ISM system, has an average CRB below 5 nm within a FOV of diameter 500 nm and below 40 nm within a FOV of diameter 1 µm.

One may expect that increasing the number of detector elements in the array, *i.e.*, for higher K values in Eq. (1-3), either the localization precision or the usable FOV increases, depending on whether, respectively, the detector element size or the overall detector size is kept constant. However, in both cases, the improvements quickly become marginal. Increasing the number of elements while keeping the element size constant, Fig. S5 (a, c), does result in a lower CRB, with the difference increasing with increasing distance from the optical axis. The 3×3 array detector has a very limited FOV of about 300 nm. For a 5×5, 7×7, and 9×9 array detector, the CRB remains stable around 5 nm up to a FOV of about 600-800 nm, and starts growing rapidly for larger FOVs. This effect, caused by the limited excitation efficiency far away from the optical axis and consequently the low SBR, shows that a 5×5 or 7×7 array detector is sufficient. Indeed, given that each detector element has a dark count rate, increasing the number of detector elements also decreases the SBR and, hence, can only be beneficial when each element collects a significant number of photons. Increasing the number of detector elements while keeping the overall detector size constant has an even smaller effect on the CRB, Fig. S5 (b, d). By imaging the emission signal with a detector array with more than 5×5 pixels, the signal is oversampled, and no significant improvement in the obtained localization precision is found.

Localizing a fluorophore with MINFLUX based techniques typically consists of two steps. In the first step, the fluorescence intensity is measured at the different TCP positions with a regularly focused laser beam. The resulting data gives a first approximation of the fluorophore position. In the second step, the MINFLUX process with a doughnut (or tophat) intensity profile is performed start-

bioRxiv preprint doi: https://doi.org/10.1101/2022.04.19.488747; this version posted April 19, 2022. The copyright holder for this preprint (which was not certified by peer review) is the author/funder, who has granted bioRxiv a license to display the preprint in perpetuity. It is made available under aCC-BY-NC-ND 4.0 International license.

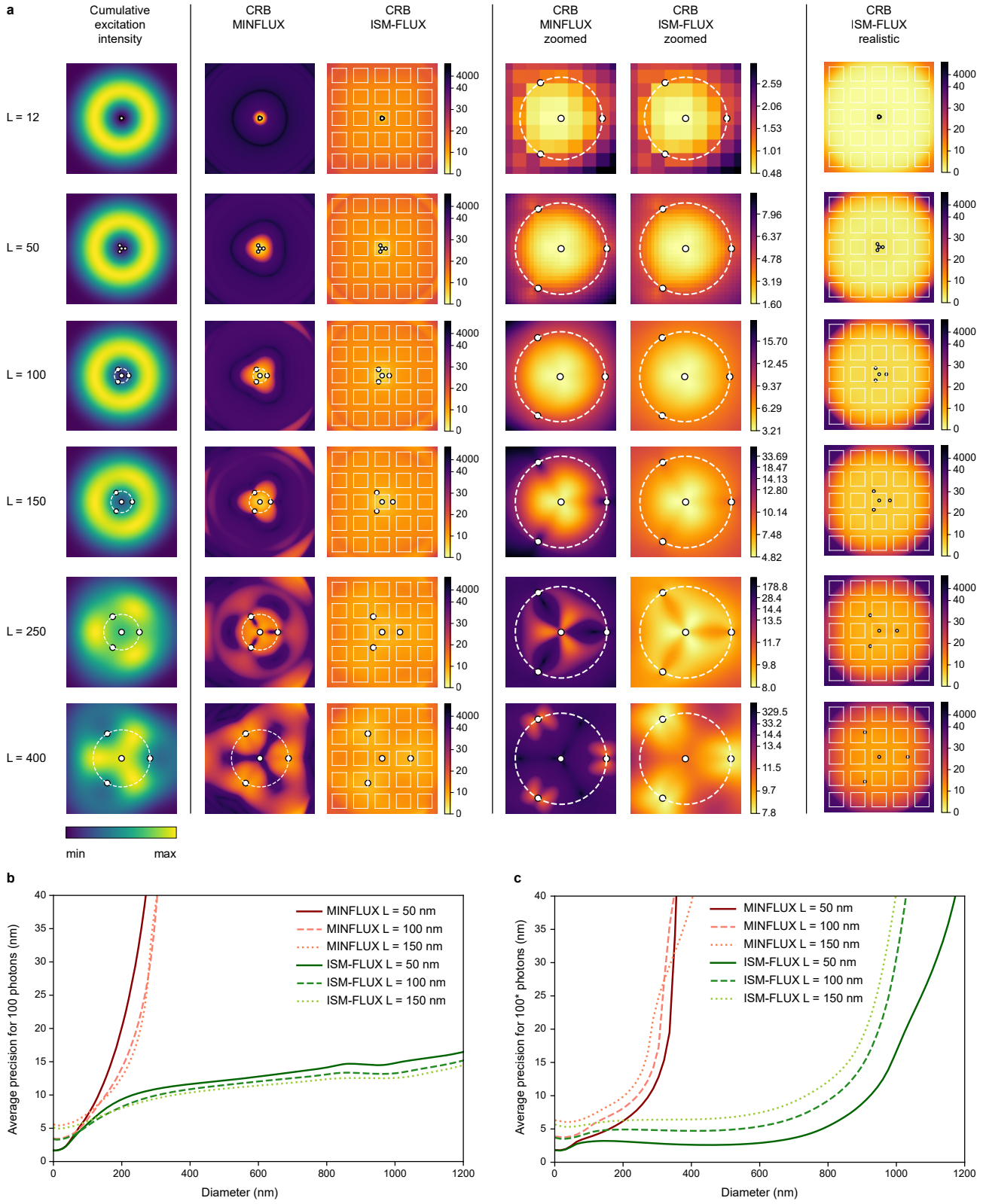

FIG. 2. (a) Sum of all four excitation doughnuts (first column) and CRB vs. L (other columns), all values in nm. The color scale switches from linear to logarithmic above 40 nm (third column) and 30 nm (last column). For the last column, the SBR was linearly scaled with the overall excitation intensity, with 100 signal counts and a SBR of 20 for the center. A constant 100 signal counts and no background was assumed for the other simulations. The white squares indicate the projection of the array detector in the sample space. 1 pixel is 2 nm. (b-c) Average CRB within a circle centered around the optical axis as a function of the circle diameter for (b) a constant number of photons and (c) a position dependent SBR, similar to (a, last column), as indicated by the asterisk in the y axis label.

bioRxiv preprint doi: https://doi.org/10.1101/2022.04.19.488747; this version posted April 19, 2022. The copyright holder for this preprint (which was not certified by peer review) is the author/funder, who has granted bioRxiv a license to display the preprint in perpetuity. It is made available under aCC-BY-NC-ND 4.0 International license.

ing at the previously estimated position and - in the case of iterative MINFLUX - decreasing L in each iteration. This approach has multiple limitations. Firstly, the pre-localization step adds experimental complexity to the technique, as the excitation beam profile has to switch from a regular beam to a doughnut beam and back. Secondly, the pre-localization step as well as the iterative approach also add computational complexity, as the molecule position has to be estimated in real-time, and the TCP has to be moved to this position (which further complicates the setup). Here, we presented ISM-FLUX, which requires neither a pre-localization step nor an iteratively updated TCP. By replacing the point-detector with a camera, a molecule can be localized over a large FOV, removing the condition that the molecule has to be within the TCP circle. For typical experimental parameters, ISM-FLUX has a homogeneous localization precision over a 600 nm FOV. In other words, if the molecule is too far from the optical axis to be localized, it is also too far from the doughnut beams to be excited in the first place. Similar to MINFLUX, the CRB decreases with decreasing L and increasing N. Our simulations show that the detector array should ideally be 5×5 or 7×7 pixels. Fewer pixels will lead to a less precise localization; more pixels will not significantly enhance the theoretical performance and will increase the dark count rate.

Asynchronous read-out SPAD array detectors are the ideal candidate for implementing ISM-FLUX. These detectors have single-photon sensitivity, no read-out noise, and a high photon timing precision, which is necessary to link each photon to one of the excitation doughnuts, especially when PIE is used. The fact that only a low number of pixels is needed allows for time-correlated single-photon counting (TC-SPC) [25]. Having access to the nanosecond-resolution arrival times makes the combination of ISM-FLUX with lifetime feasible, which can give extra information on the macromolecular structure or its microenvironment and allows for multiplexing. In the context of single-particle tracking, the high timing precision of SPADs may be exploited to study microsecond-scale dynamics with ISM-FLUX.

We predict that the main advantage of ISM-FLUX will be the simplicity of the experimental implementation. Indeed, our simulations show that current SPAD based ISM setups [22, 26, 27] require only minor modifications for ISM-FLUX measurements. On the excitation side, the conventional laser line can be replaced with four lines in PIE mode, focused at the four positions of the TCP. On the detection side, it is sufficient to update the data acquisition protocol such that each photon can be linked to one of the doughnut beams. The magnification on the detector can be the same as in ISM, *i.e.*, each side of the detector corresponds to about 1 to 1.5 Airy units. In addition to a good localization precision and large FOV, this magnification also has the optical sectioning effect, which is important for 3D samples or for keeping the background low in samples with DNA-PAINT based blinking.

In summary, ISM-FLUX provides an elegant solution to some of the experimental challenges of MINFLUX based techniques while maintaining the nanometer scale spatial resolution and the combination with time-resolved imaging. We are convinced that these advantages will trigger many labs to develop ISM-FLUX microscopes and help localization microscopy with nanometer precision to become routine.

ACKNOWLEDGMENTS

The authors thank Dr. Giorgio Tortarolo, Alessandro Zunino, Andrea Bucci, Francesco Fersini, and Simone Civita for the useful discussions and Fernando Caprile and Dr. Luciano Masullo for their kind assistance with the use of the Python package PyCustomFocus. This research was supported by the European Research Council, Bright Eyes no. 818699 (G.V.) and by the European Union's Horizon 2020 research and innovation programme under the Marie Sk1odowska-Curie grant agreement no. 890923 (SMSPAD) (E.S.).

[1] M. J. Rust, M. Bates, and X. W. Zhuang, Sub-diffraction-limit imaging by stochastic optical reconstruction microscopy (storm), Nat. Methods **3**, 793 (2006).

[2] M. Heilemann, S. van de Linde, M. Schuttpelz, R. Kasper, B. Seefeldt, A. Mukherjee, P. Tinnefeld, and M. Sauer, Subdiffraction-resolution fluorescence imaging with conventional fluorescent probes, Angewandte Chemie-International Edition **47**, 6172 (2008).

[3] E. Betzig, G. H. Patterson, R. Sougrat, O. W. Lindwasser, S. Olenych, J. S. Bonifacino, M. W. Davidson, J. Lippincott-Schwartz, and H. F. Hess, Imaging intracellular fluorescent proteins at nanometer resolution, Science **313**, 1642 (2006).

[4] S. T. Hess, T. P. Girirajan, and M. D. Mason, Ultra-high resolution imaging by fluorescence photoactivation localization microscopy, Biophys. J. **91**, 4258 (2006).

[5] A. Sharonov and R. M. Hochstrasser, Wide-field subdiffraction imaging by accumulated binding of diffusing probes, Proc. Natl. Acad. Sci. U. S. A. **103**, 18911 (2006).

[6] L. Schermelleh, A. Ferrand, T. Huser, C. Eggeling, M. Sauer, O. Biehlmaier, and G. P. C. Drummen, Super-resolution microscopy demystified, Nature Cell Biology **21**, 72 (2019).

[7] M. Sauer and M. Heilemann, Single-molecule localization microscopy in eukaryotes, Chem Rev **117**, 7478 (2017).

[8] J. Engelhardt, J. Keller, P. Hoyer, M. Reuss, T. Staudt, and S. W. Hell, Molecular orientation affects localization accuracy in superresolution far-field fluorescence microscopy, Nano Lett. **11**, 209 (2011).

[9] M. Lelek, M. T. Gyparaki, G. Beliu, F. Schueder, J. Griffié, S. Manley, R. Jungmann, M. Sauer, M. Lakadamyali, and C. Zimmer, Single-molecule local-

bioRxiv preprint doi: https://doi.org/10.1101/2022.04.19.488747; this version posted April 19, 2022. The copyright holder for this preprint (which was not certified by peer review) is the author/funder, who has granted bioRxiv a license to display the preprint in perpetuity. It is made available under aCC-BY-NC-ND 4.0 International license.

ization microscopy, Nat. Rev. Methods Primers **1**, 39 (2021).

[10] J. Schnitzbauer, M. T. Strauss, T. Schlichthaerle, F. Schueder, and R. Jungmann, Super-resolution microscopy with dna-paint, Nat. Protoc. **12**, 1198 (2017).

[11] M. Dai, R. Jungmann, and P. Yin, Optical imaging of individual biomolecules in densely packed clusters, Nat. Nanotechnol. **11**, 798 (2016).

[12] N. Oleksiievets, Y. Sargsyan, J. C. Thiele, N. Mougios, S. Sograte-Idrissi, O. Nevskyi, I. Gregor, F. Opazo, S. Thoms, J. Enderlein, and R. Tsukanov, Fluorescence lifetime dna-paint for multiplexed super-resolution imaging of cells, Commun. Biol. **5**, 38 (2022).

[13] A. C. Ulku, C. Bruschini, I. M. Antolovic, E. Charbon, Y. Kuo, R. Ankri, S. Weiss, and X. Michalet, A 512x512 spad image sensor with integrated gating for widefield flim, IEEE J. Sel. Top. Quant. **25** (2019).

[14] F. Balzarotti, Y. Eilers, K. C. Gwosch, A. H. Gynna, V. Westphal, F. D. Stefani, J. Elf, and S. W. Hell, Nanometer resolution imaging and tracking of fluorescent molecules with minimal photon fluxes, Science **355**, 606 (2017).

[15] M. Weber, M. Leutenegger, S. Stoldt, S. Jakobs, T. S. Mihaila, A. N. Butkevich, and S. W. Hell, Minsted fluorescence localization and nanoscopy, Nat. Photonics **15**, 361 (2021).

[16] L. A. Masullo, F. Steiner, J. Zähringer, L. F. Lopez, J. Bohlen, L. Richter, F. Cole, P. Tinnefeld, and F. D. Stefani, Pulsed interleaved minflux, Nano Lett. **21**, 840 (2021).

[17] K. Zhao, X. Xu, W. Ren, D. Jin, and P. Xi, Two-photon minflux with doubled localization precision, eLight **2**, 5 (2022).

[18] J. C. Thiele, D. A. Helmerich, N. Oleksiievets, R. Tsukanov, E. Butkevich, M. Sauer, O. Nevskyi, and J. Enderlein, Confocal fluorescence-lifetime single-molecule localization microscopy, ACS Nano **14**, 14190–14200 (2020).

[19] K. C. Gwosch, J. K. Pape, F. Balzarotti, P. Hoess, J. Ellenberg, J. Ries, and S. W. Hell, Minflux nanoscopy delivers 3d multicolor nanometer resolution in cells, Nat. Methods **17**, 217 (2020).

[20] R. Schmidt, T. Weihs, C. A. Wurm, I. Jansen, J. Rehman, S. J. Sahl, and S. W. Hell, Minflux nanometer-scale 3d imaging and microsecond-range tracking on a common fluorescence microscope, Nat. Commun. **12**, 1478 (2021).

[21] M. Castello, C. J. R. Sheppard, A. Diaspro, and G. Vicidomini, Image scanning microscopy with a quadrant detector, Opt. Lett. **40**, 5355 (2015).

[22] M. Castello, G. Tortarolo, M. Buttafava, T. Deguchi, F. Villa, S. Koho, L. Pesce, M. Oneto, S. Pelicci, L. Lanzano, P. Bianchini, C. J. R. Sheppard, A. Diaspro, A. Tosi, and G. Vicidomini, A robust and versatile platform for image scanning microscopy enabling super-resolution flim, Nat. Methods **16**, 1 (2019).

[23] L. Gu, Y. Li, S. Zhang, Y. Xue, W. Li, D. Li, T. Xu, and W. Ji, Molecular resolution imaging by repetitive optical selective exposure, Nat. Methods **16**, 1114 (2019).

[24] J. Cnossen, T. Hinsdale, R. Thorsen, M. Siemons, F. Schueder, R. Jungmann, C. S. Smith, B. Rieger, and S. Stallinga, Localization microscopy at doubled precision with patterned illumination, Nat. Methods **17**, 59 (2020).

[25] A. Rossetta, E. Slenders, M. Donato, E. Perego, F. Diotalevi, L. Lanzanó, S. Koho, G. Tortarolo, M. Crepaldi, and G. Vicidomini, The brighteyes-ttm: an open-source time-tagging module for single-photon microscopy, BioRxiv (2021).

[26] E. Slenders, M. Castello, M. Buttafava, F. Villa, A. Tosi, L. Lanzanò, S. Koho, and G. Vicidomini, Confocal-based fluorescence fluctuation spectroscopy with a spad array detector, Light-Sci. Appl. **10**, 31 (2021).

[27] E. Slenders, E. Perego, M. Buttafava, G. Tortarolo, E. Conca, S. Zappone, A. Pierzynska-Mach, F. Villa, E. M. Petrini, A. Barberis, A. Tosi, and G. Vicidomini, Cooled spad array detector for low light-dose fluorescence laser scanning microscopy, Biophys. Rep. **1**, 1 (2021).

bioRxiv preprint doi: https://doi.org/10.1101/2022.04.19.488747; this version posted April 19, 2022. The copyright holder for this preprint (which was not certified by peer review) is the author/funder, who has granted bioRxiv a license to display the preprint in perpetuity. It is made available under aCC-BY-NC-ND 4.0 International license.

SUPPORTING INFORMATION

Supplementary Note 1: analytical calculation Cramér-Rao bound

We calculate the CR bound analytically for a molecule close to the center of the detector, i.e. $(x_0, y_0) \to (0,0)$. We define the doughnut beams at positions (p_i, q_i) (i = 1,...,K) as the product of a second order polynomial with a Gaussian. Then, for doughnuts close to the optical axis ($(p_i, q_i) \to (0,0)$), the excitation intensity is:

$$I_{ex,i}(x_0, y_0) = A\left[(p_i - x_0)^2 + (q_i - y_0)^2\right] \exp\left(\frac{-4\ln(2)\left[(p_i - x_0)^2 + (q_i - y_0)^2\right]}{\sigma_0^2}\right) \tag{1}$$

$$= AD_{i,0} \exp\left(\frac{-4\ln(2) D_{i,0}}{\sigma_0^2}\right) \approx AD_{i,0}, \tag{2}$$

with A a scaling factor, σ_0^2 describing the doughnut diameter, and $D_{i,0}$ the shorthand notation for the squared distance between doughnut i and the molecule position: $(p_i - x_0)^2 + (q_i - y_0)^2$.

We approximate the emission PSF by a $2D$ Gaussian with standard deviation σ.

Under the assumption that the detected fluorescence intensity is proportional to the excitation intensity, the expected relative number of photons that will be detected by each pixel of the array detector under illumination of doughnut i (p_i) is proportional to the product of the excitation intensity and the emission PSF centered around position (x_0, y_0):

$$p_i = \frac{AD_{i,0}\frac{1}{2\pi\sigma^2}\exp\left(-\frac{(x-x_0)^2+(y-y_0)^2}{2\sigma^2}\right)dxdy}{\iint \sum_i AD_{i,0}\frac{1}{2\pi\sigma^2}\exp\left(-\frac{(x-x_0)^2+(y-y_0)^2}{2\sigma^2}\right)dxdy} \tag{3}$$

$$= \frac{D_{i,0}\exp\left(-\frac{(x-x_0)^2+(y-y_0)^2}{2\sigma^2}\right)dxdy}{\iint \sum_i D_{i,0}\exp\left(-\frac{(x-x_0)^2+(y-y_0)^2}{2\sigma^2}\right)dxdy} = \frac{T}{B}, \tag{4}$$

with T the numerator and B the denominator. We assume an infinitely large detector (which is reasonable if the detector is larger than the emission PSF and the molecule is close to the optical axis) with infinitely small pixels. We omit the factor $dxdy$ in T to work with photon *densities*.

To calculate the CRB, we need the partial derivatives of p_i to x_0 and y_0. We first calculate the derivatives of T and B.

$$\frac{\partial T}{\partial x_0} = \frac{\partial D_{i,0}}{\partial x_0}\exp\left(-\frac{(x-x_0)^2+(y-y_0)^2}{2\sigma^2}\right) + D_{i,0}\exp\left(-\frac{(x-x_0)^2+(y-y_0)^2}{2\sigma^2}\right)\frac{x-x_0}{\sigma^2} \tag{5}$$

$$= \exp\left(-\frac{(x-x_0)^2+(y-y_0)^2}{2\sigma^2}\right)\left[-2(p_i - x_0) + D_{i,0}\frac{(x-x_0)}{\sigma^2}\right]; \tag{6}$$

$$B = \sum_i D_{i,0}\iint \exp\left(-\frac{(x-x_0)^2+(y-y_0)^2}{2\sigma^2}\right)dxdy = 2\pi\sigma^2\sum_i (p_i - x_0)^2 + (q_i - y_0)^2 \tag{7}$$

$$\Rightarrow \frac{\partial B}{\partial x_0} = -4\pi\sigma^2\sum_i (p_i - x_0) \tag{8}$$

$$\Rightarrow \frac{\partial p_i}{\partial x_0} = \frac{1}{B}\frac{\partial T}{\partial x_0} - \frac{T}{B^2}\frac{\partial B}{\partial x_0} \tag{9}$$

$$= \frac{\exp\left(-\frac{(x-x_0)^2+(y-y_0)^2}{2\sigma^2}\right)\left[-2(p_i - x_0) + D_{i,0}\frac{(x-x_0)}{\sigma^2}\right]}{2\pi\sigma^2\sum_i (p_i - x_0)^2 + (q_i - y_0)^2} \tag{10}$$

$$- \frac{D_{i,0}\exp\left(-\frac{(x-x_0)^2+(y-y_0)^2}{2\sigma^2}\right)\left[-4\pi\sigma^2\sum_i (p_i - x_0)\right]}{4\pi^2\sigma^4\left[\sum_i (p_i - x_0)^2 + (q_i - y_0)^2\right]^2}. \tag{11}$$

bioRxiv preprint doi: https://doi.org/10.1101/2022.04.19.488747; this version posted April 19, 2022. The copyright holder for this preprint (which was not certified by peer review) is the author/funder, who has granted bioRxiv a license to display the preprint in perpetuity. It is made available under aCC-BY-NC-ND 4.0 International license.

For a molecule on the optical axis, we have $(x_0, y_0) = (0, 0)$ and $\sum_i (p_i - x_0) = \sum_i p_i = 0$ for a symmetric TCP. Computing $\frac{\partial p_i}{\partial x_0}$, we find (and for symmetry reasons also for $\frac{\partial p_i}{\partial y_0}$):

$$\frac{\partial p_i}{\partial x_0} = \frac{\exp\left(-\frac{x^2+y^2}{2\sigma^2}\right)\left[-2p_i + (p_i^2+q_i^2)\frac{x}{\sigma^2}\right]}{2\pi\sigma^2 \sum_i (p_i^2+q_i^2)}; \tag{12}$$

$$\frac{\partial p_i}{\partial y_0} = \frac{\exp\left(-\frac{x^2+y^2}{2\sigma^2}\right)\left[-2q_i + (p_i^2+q_i^2)\frac{y}{\sigma^2}\right]}{2\pi\sigma^2 \sum_i (p_i^2+q_i^2)}. \tag{13}$$

Next, we calculate the following three terms for a molecule on the optical axis: $\iint \sum_i \frac{1}{p_i}\left[\left(\frac{\partial p_i}{\partial x_0}\right)^2 + \left(\frac{\partial p_i}{\partial y_0}\right)^2\right] dxdy$, $\iint \sum_i \frac{1}{p_i}\left(\frac{\partial p_i}{\partial x_0}\right)^2 dxdy$, and $\iint \sum_i \frac{\partial p_i}{\partial x_0}\frac{\partial p_i}{\partial y_0} dxdy$:

$$\begin{aligned}
\iint \sum_i \frac{1}{p_i}\left[\left(\frac{\partial p_i}{\partial x_0}\right)^2 + \left(\frac{\partial p_i}{\partial y_0}\right)^2\right] dxdy &= \iint \sum_i \frac{B}{T}\frac{1}{4\pi^2\sigma^4}\frac{\exp\left(-\frac{x^2+y^2}{\sigma^2}\right)\left[-2p_i + (p_i^2+q_i^2)\frac{x}{\sigma^2}\right]^2}{\left[\sum_i (p_i^2+q_i^2)\right]^2} \\
&\quad + \frac{B}{T}\frac{1}{4\pi^2\sigma^4}\frac{\exp\left(-\frac{x^2+y^2}{\sigma^2}\right)\left[-2q_i + (p_i^2+q_i^2)\frac{y}{\sigma^2}\right]^2}{\left[\sum_i (p_i^2+q_i^2)\right]^2} dxdy && (14) \\
&= \iint \sum_i \frac{B}{T}\frac{\exp\left(-\frac{x^2+y^2}{\sigma^2}\right)}{4\pi^2\sigma^4\left(\sum_i R_i^2\right)^2}\left[\left(-2p_i + R_i^2\frac{x}{\sigma^2}\right)^2 + \left(-2q_i + R_i^2\frac{y}{\sigma^2}\right)^2\right] dxdy && (15) \\
&= \iint \sum_i \frac{2\exp\left(-\frac{x^2+y^2}{2\sigma^2}\right)}{3\pi\sigma^2 L^2 R_i^2}\left(4R_i^2 - \frac{4p_i R_i^2 x}{\sigma^2} + \frac{R_i^4 x^2}{\sigma^4} - \frac{4q_i R_i^2 y}{\sigma^2} + \frac{R_i^4 y^2}{\sigma^4}\right) dxdy && (16) \\
&= \sum_i \iint \frac{8\exp\left(-\frac{x^2+y^2}{2\sigma^2}\right)}{3\pi\sigma^2 L^4}\left(L^2 - \frac{p_i L^2 x}{\sigma^2} + \frac{L^4 x^2}{16\sigma^4} - \frac{q_i L^2 y}{\sigma^2} + \frac{L^4 y^2}{16\sigma^4}\right) dxdy && (17) \\
&= \iint \frac{8\exp\left(-\frac{x^2+y^2}{2\sigma^2}\right)}{\pi\sigma^2 L^2} dxdy = \frac{16}{L^2}, && (18)
\end{aligned}$$

where $p_i^2 + q_i^2 = R_i^2$. We made use of the fact that the integral of an odd function over $\mathbb{R}$ is 0 (if finite), the TCP pattern consists of three positions uniformly distributed on a circle with radius $L/2$ centered around the optical axis, $B = \frac{3}{2}\pi\sigma^2 L^2$, $T = R_i^2 \exp\left(-\frac{x^2+y^2}{2\sigma^2}\right)$, and $L \ll \sigma$. We apply the same assumptions to the other terms:

bioRxiv preprint doi: https://doi.org/10.1101/2022.04.19.488747; this version posted April 19, 2022. The copyright holder for this preprint (which was not certified by peer review) is the author/funder, who has granted bioRxiv a license to display the preprint in perpetuity. It is made available under aCC-BY-NC-ND 4.0 International license.

$$\iint \sum_i \frac{1}{p_i}\left(\frac{\partial p_i}{\partial x_0}\right)^2 dxdy = \iint \sum_i \frac{2}{R_i^2 \exp\left(-\frac{x^2+y^2}{2\sigma^2}\right)} \frac{\exp\left(-\frac{x^2+y^2}{\sigma^2}\right)\left(-2p_i + \left(p_i^2+q_i^2\right)\frac{x}{\sigma^2}\right)^2}{3\pi\sigma^2 L^2} dxdy \tag{19}$$

$$= \iint \sum_i \frac{2\exp\left(-\frac{x^2+y^2}{2\sigma^2}\right)}{3\pi\sigma^2 L^2 R_i^2} 4p_i^2 dxdy \tag{20}$$

$$= \iint \frac{8\exp\left(-\frac{x^2+y^2}{2\sigma^2}\right)}{3\pi\sigma^2 L^2 L^2/4} \frac{3L^2}{16} 2dxdy \tag{21}$$

$$= \iint \frac{4\exp\left(-\frac{x^2+y^2}{2\sigma^2}\right)}{\pi\sigma^2 L^2} dxdy = \frac{8}{L^2} \tag{22}$$

$$\frac{\partial p_i}{\partial x_0}\frac{\partial p_i}{\partial y_0} = \frac{\exp\left(-\frac{x^2+y^2}{2\sigma^2}\right)\left(-2p_i + \left(p_i^2+q_i^2\right)\frac{x}{\sigma^2}\right)}{2\pi\sigma^2 \sum_i \left(p_i^2+q_i^2\right)} \frac{\exp\left(-\frac{x^2+y^2}{2\sigma^2}\right)\left[-2q_i + \left(p_i^2+q_i^2\right)\frac{y}{\sigma^2}\right]}{2\pi\sigma^2 \sum_i \left(p_i^2+q_i^2\right)} \tag{23}$$

$$= \frac{4\exp\left(-\frac{x^2+y^2}{\sigma^2}\right)\left(-2p_i + \frac{L^2 x}{4\sigma^2}\right)\left(-2q_i + \frac{L^2 y}{4\sigma^2}\right)}{9\pi^2\sigma^4 L^4} \tag{24}$$

$$\Rightarrow \iint \frac{\partial p_i}{\partial x_0}\frac{\partial p_i}{\partial y_0} dxdy = \frac{4\exp\left(-\frac{x^2+y^2}{\sigma^2}\right)4p_i q_i}{9\pi^2\sigma^4 L^4} dxdy \tag{25}$$

$$= \iint \frac{16\exp\left(-\frac{x^2+y^2}{\sigma^2}\right)p_i q_i}{9\pi^2\sigma^4 L^4} dxdy = 0 \tag{26}$$

$$\Rightarrow \tilde{\sigma}_{CRB} = \sqrt{\frac{1}{2N}\frac{\iint \sum_i \frac{1}{p_i}\left[\left(\frac{\partial p_i}{\partial y}\right)^2 + \left(\frac{\partial p_i}{\partial x}\right)^2\right] dxdy}{\left[\iint \sum_{i=0} \frac{1}{p_i}\left(\frac{\partial p_i}{\partial x}\right)^2 dxdy\right]\left[\iint \sum_i \frac{1}{p_i}\left(\frac{\partial p_i}{\partial y}\right)^2 dxdy\right] - \left[\iint \sum_i \frac{1\partial p_i \partial p_i}{p_i \partial x \partial y} dxdy\right]^2}} \tag{27}$$

$$= \sqrt{\frac{1}{2N}\frac{16/L^2}{\left(8/L^2\right)\left(8/L^2\right)}} = \frac{L}{2\sqrt{2N}} \tag{28}$$

bioRxiv preprint doi: https://doi.org/10.1101/2022.04.19.488747; this version posted April 19, 2022. The copyright holder for this preprint (which was not certified by peer review) is the author/funder, who has granted bioRxiv a license to display the preprint in perpetuity. It is made available under aCC-BY-NC-ND 4.0 International license.

Supplementary Note 2: simulation settings

We assumed an excitation and emission wavelength of respectively 640 nm and 680 nm and an objective NA of 1.4. The pixel size of the simulation space, and hence of all the CRB images, was 2 nm. Unless stated otherwise, each detector element was a square of size 50 µm with a pitch (distance between the centers of two adjacent elements) of 75 µm and the overall magnification was 500x.

The MDFs for the different combinations of excitation pattern and detector element position were simulated in Python. The MDF is $h_1 \cdot (h_2 * p)$, with h_1 the doughnut excitation pattern, obtained with the PyCustomFocus library with the mask set to a vortex phase plate, h_2 the detection (or emission) PSF, calculated with the PyCustomFocus library, $*$ the convolution product and p the 2D window function for the corresponding detector element. The different excitation patterns were obtained by shifting h_1 in x and y to the four positions of the TCP.

We calculated the localization precision $\sigma_{\mathrm{CRB}}(\mathbf{r}_E))$ using Eq. 4 (main text) by numerically calculating $p_i(\mathbf{r}_E)$ (Eq. 2) and its derivatives.

bioRxiv preprint doi: https://doi.org/10.1101/2022.04.19.488747; this version posted April 19, 2022. The copyright holder for this preprint (which was not certified by peer review) is the author/funder, who has granted bioRxiv a license to display the preprint in perpetuity. It is made available under aCC-BY-NC-ND 4.0 International license.

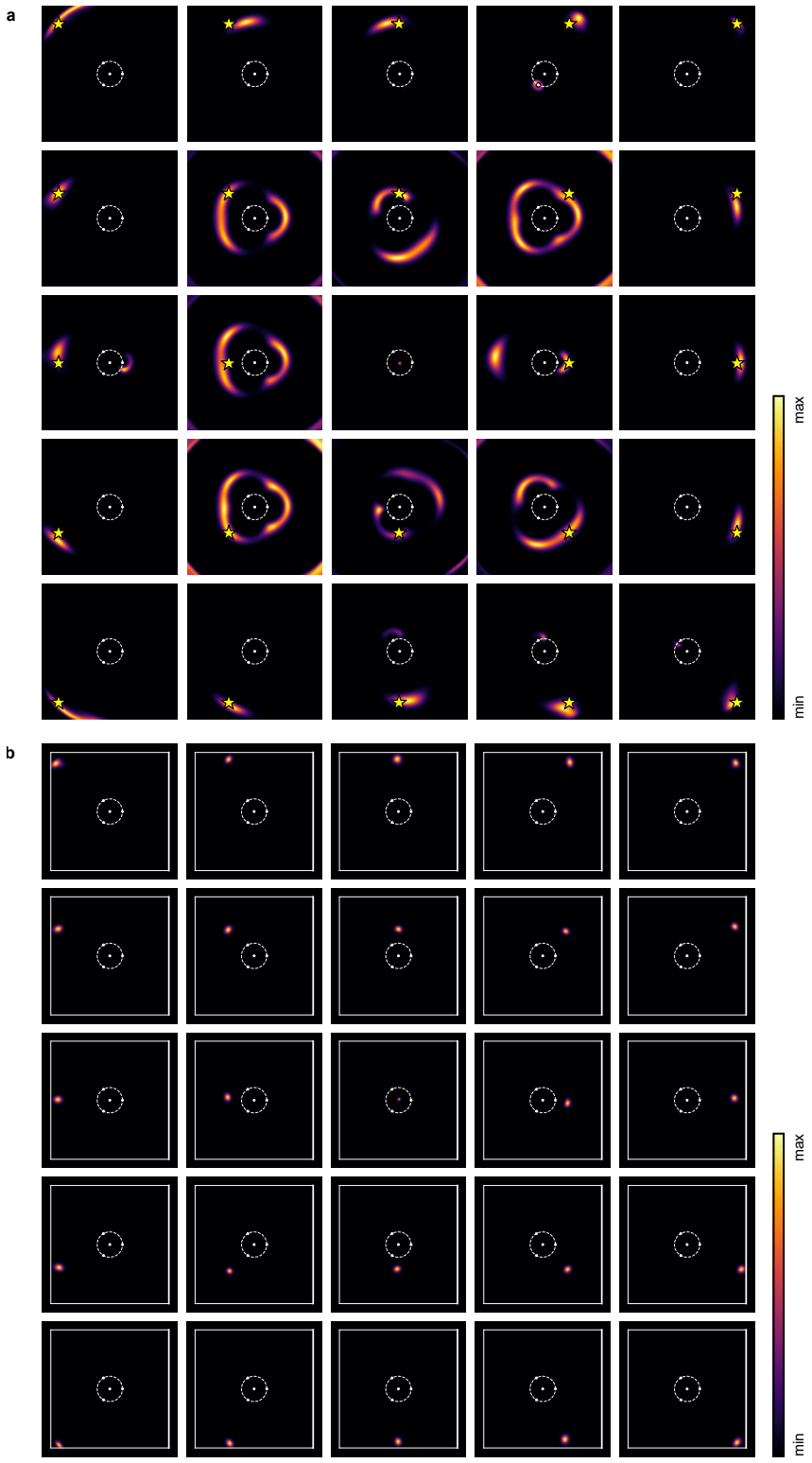

Figure S1: Simulated likelihood functions for (a) MINFLUX and (b) ISM-FLUX for different positions of the fluorophore (yellow star). Simulation settings: 100 signal counts, no background. The circle indicates the TCP, L = 150 nm. For visualization purposes, the fluorophores are not shown in all plots. All images show a FOV of 800 nm.

bioRxiv preprint doi: https://doi.org/10.1101/2022.04.19.488747; this version posted April 19, 2022. The copyright holder for this preprint (which was not certified by peer review) is the author/funder, who has granted bioRxiv a license to display the preprint in perpetuity. It is made available under aCC-BY-NC-ND 4.0 International license.

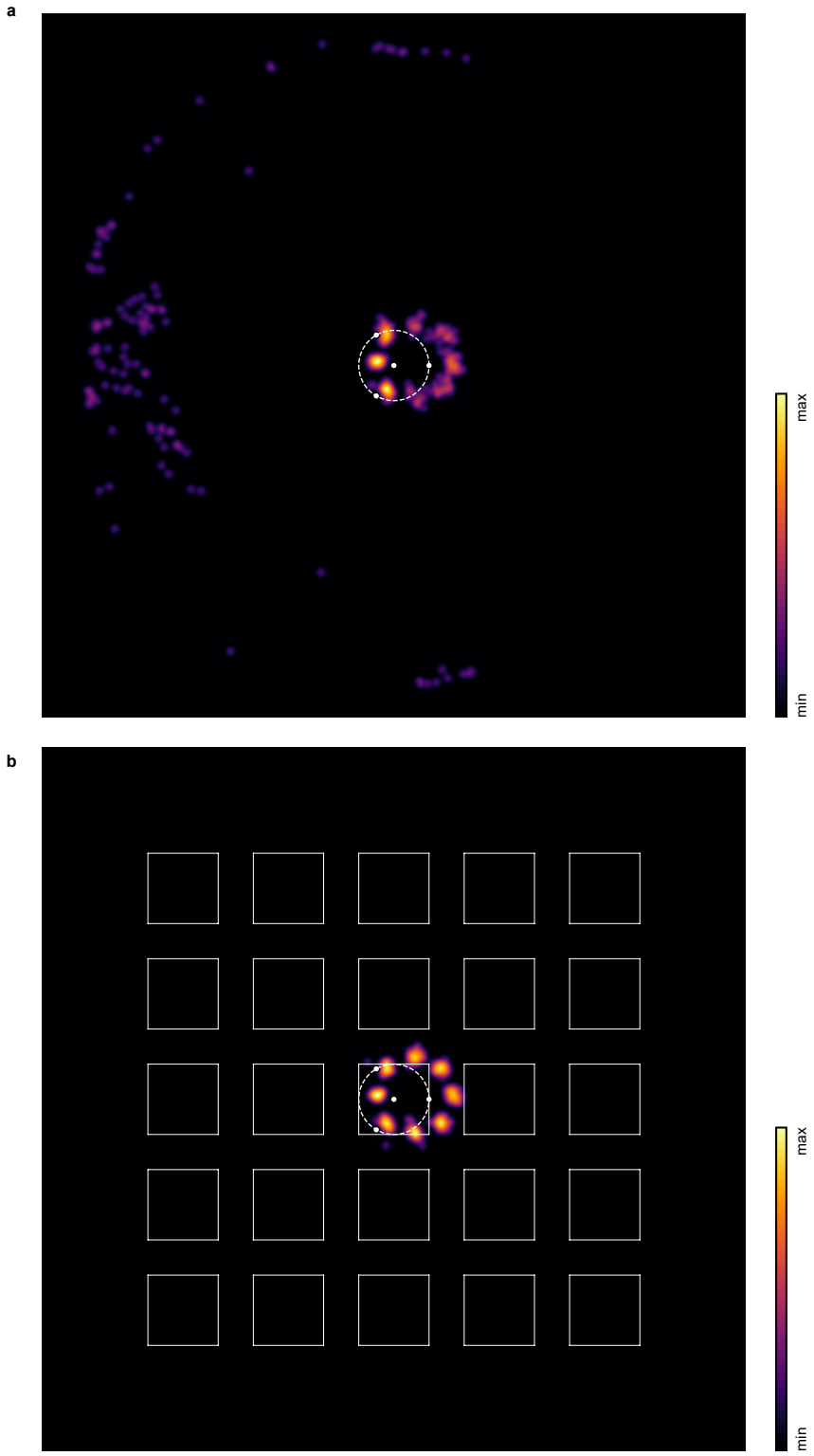

Figure S2: Simulated images of a nuclear pore complex, consisting of eight units located in a regular pattern on a circle of diameter 110 nm with (a) a single-element detector and (b) an array detector. The TCP is kept fixed for all localizations, centered around the optical axis with $L = 100$ nm. Sum over 50 localizations per molecule, each localization performed with between 125 photons (close to the optical axis) and 376 photons (farther away from the optical axis), photon counts linearly scaled with the excitation intensity, no background assumed. Localizations convolved with a 2D Gaussian with $\sigma = 2$ pixels (4 nm). Logarithmic color map.

bioRxiv preprint doi: https://doi.org/10.1101/2022.04.19.488747; this version posted April 19, 2022. The copyright holder for this preprint (which was not certified by peer review) is the author/funder, who has granted bioRxiv a license to display the preprint in perpetuity. It is made available under aCC-BY-NC-ND 4.0 International license.

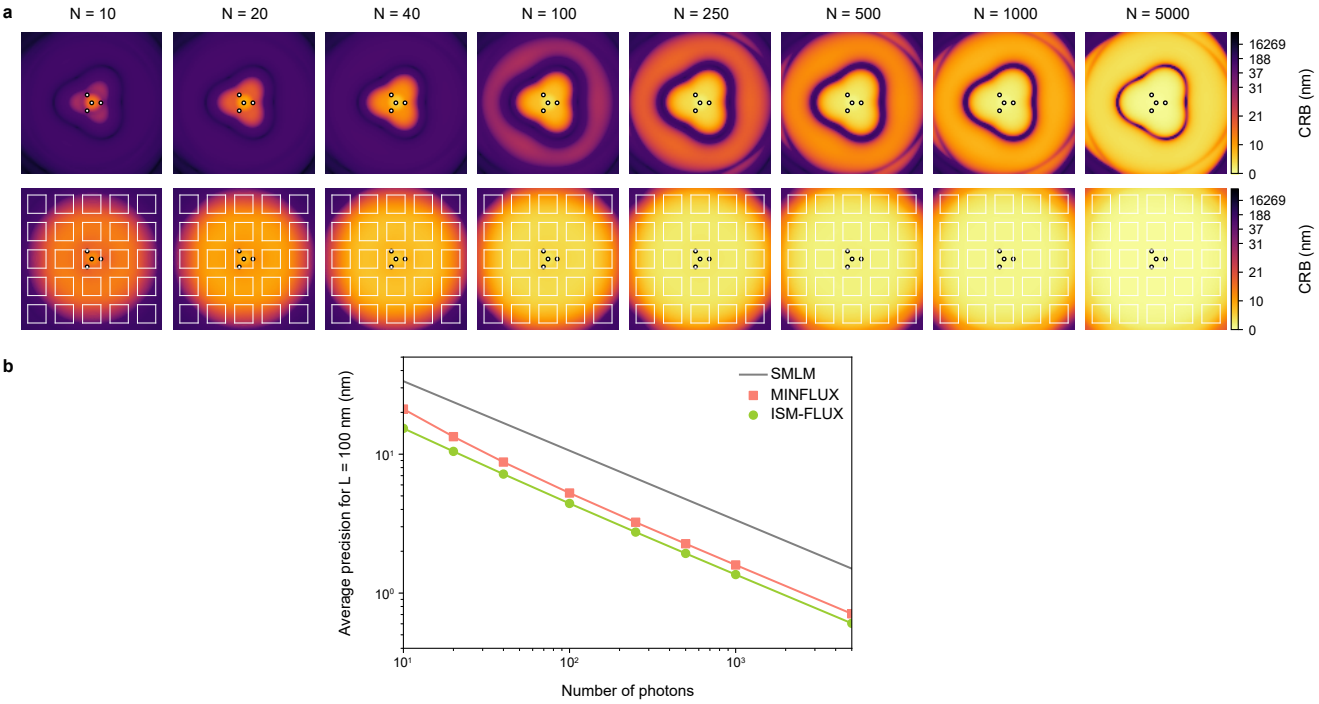

Figure S3: (a) MINFLUX CRB (top) and ISM-FLUX CRB (bottom) as a function of the number of emission photons. (b) Average CRB within the TCP circle. Simulation settings: L = 100 nm, SBR linearly scaled with the overall excitation intensity, with N signal counts and 5 background counts for the center.

bioRxiv preprint doi: https://doi.org/10.1101/2022.04.19.488747; this version posted April 19, 2022. The copyright holder for this preprint (which was not certified by peer review) is the author/funder, who has granted bioRxiv a license to display the preprint in perpetuity. It is made available under aCC-BY-NC-ND 4.0 International license.

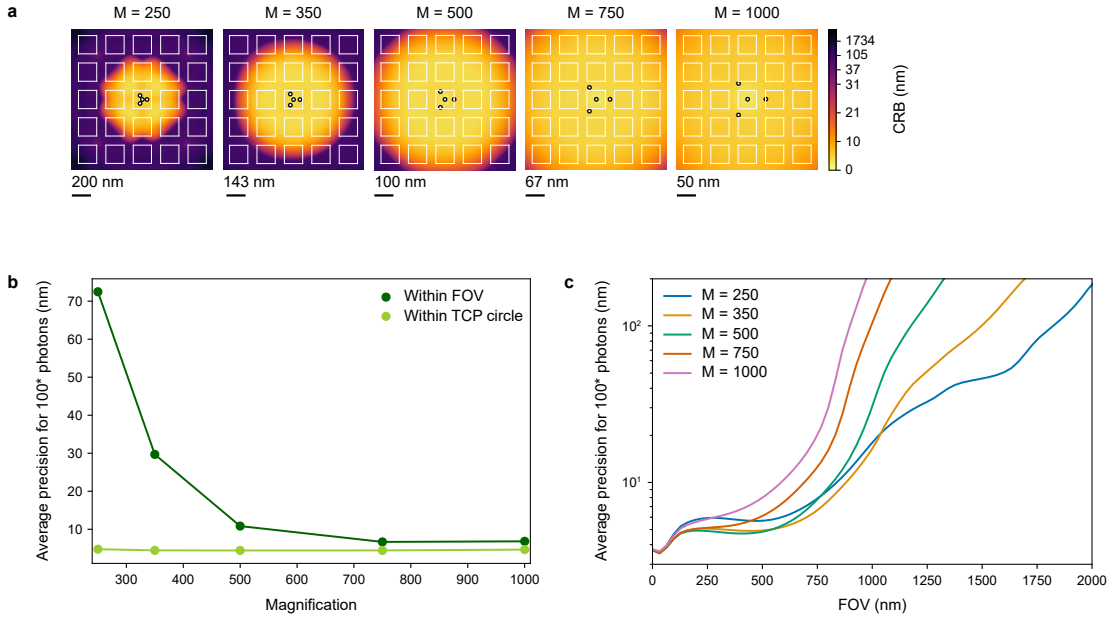

Figure S4: (a) ISM-FLUX CRB as a function of the system magnification. Simulation settings: L = 100 nm, SBR linearly scaled with the overall excitation intensity, with 100 signal counts and a SBR of 20 for the center.

bioRxiv preprint doi: https://doi.org/10.1101/2022.04.19.488747; this version posted April 19, 2022. The copyright holder for this preprint (which was not certified by peer review) is the author/funder, who has granted bioRxiv a license to display the preprint in perpetuity. It is made available under aCC-BY-NC-ND 4.0 International license.

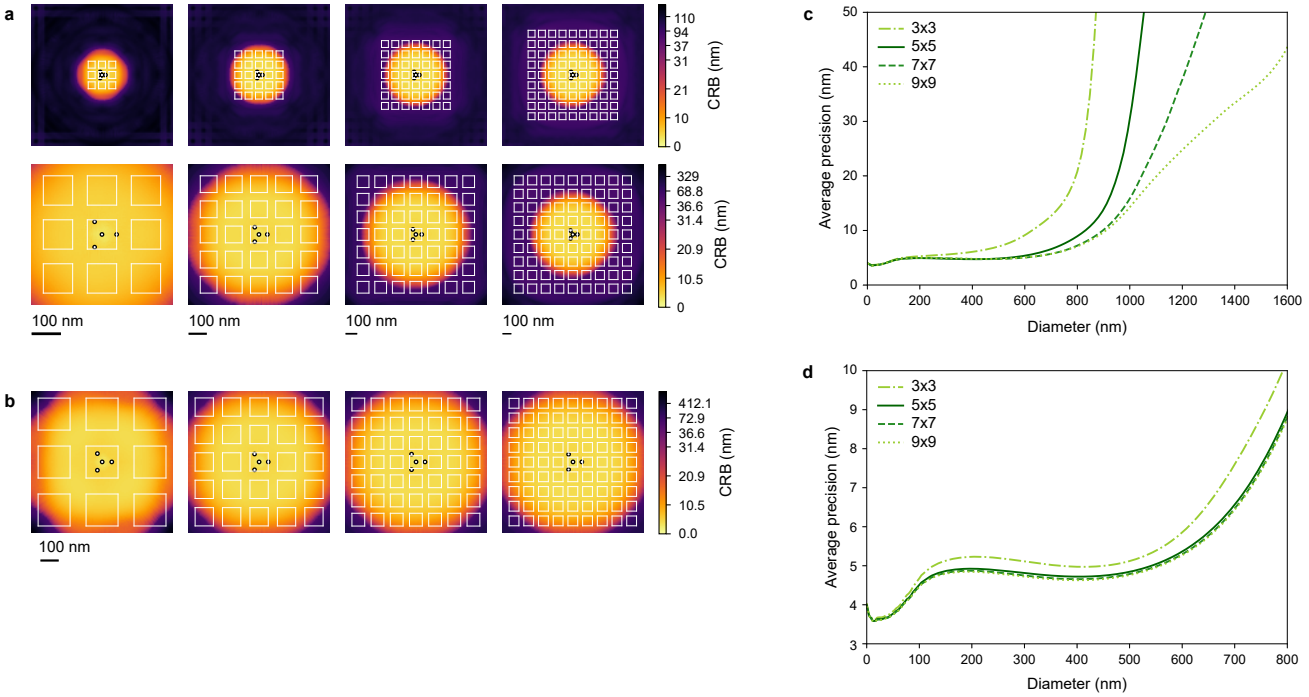

Figure S5: ISM-FLUX CRB for different numbers of detector elements in the array with (a, c) a constant detector element size and (b, d) a constant overall detector size. Simulation settings: L = 100 nm, M = 500×, SBR linearly scaled with the overall excitation intensity, with 100 signal counts and a SBR of 20 for the center.